Journal of Power Sources 195 (2010) 4804–4810

Contents lists available at ScienceDirect

Journal of Power Sources

journal homepage: www.elsevier.com/locate/jpowsour

Microstructural analysis of a solid oxide fuel cell anode using focused ion beam techniques coupled with electrochemical simulation

P.R. Shearing, Q. Cai, J.I. Golbert, V. Yufit, C.S. Adjiman, N.P. Brandon*

Imperial College, London SW7 2AZ, UK

ARTICLE INFO

Article history:
Received 13 October 2009
Received in revised form 11 February 2010
Accepted 13 February 2010
Available online 23 February 2010

Keywords:
Solid oxide fuel cell
Tomography
Microstructure
Anode

ABSTRACT

Porous composite electrodes play a critical role in determining the performance and durability of solid oxide fuel cells, which are now emerging as a high efficiency, low emission energy conversion technology for a wide range of applications.

In this paper we present work to combine experimental electrochemical and microstructural characterisation with electrochemical simulation to characterise a porous solid oxide fuel cell anode. Using a standard, electrolyte supported, screen printed Ni–YSZ anode, electrochemical impedance spectroscopy has been conducted in a symmetrical cell configuration. The electrode microstructure has been characterised using FIB tomography and the resulting microstructure has been used as the basis for electrochemical simulation. The outputs from this simulation have in turn been compared to the results of the electrochemical experiments.

A sample of an SOFC anode of 6.68 $\mu m \times 5.04\ \mu m \times 1.50\ \mu m$ in size was imaged in three dimensions using FIB tomography and the total triple phase boundary density was found to be 13 μm^{-2}. The extracted length-specific exchange current for hydrogen oxidation (97% H_2, 3% H_2O) at a Ni–YSZ anode was found to be 0.94×10^{-10}, 2.14×10^{-10}, and 12.2×10^{-10} A μm^{-1} at 800, 900 and 1000 °C, respectively, consistent with equivalent literature data for length-specific exchange currents for hydrogen at geometrically defined nickel electrodes on YSZ electrolytes.

1. Introduction

Porous composite electrodes play a critical role in determining the performance and durability of solid oxide fuel cells (SOFCs), which are now emerging as a high efficiency, low emission energy conversion technology for a wide range of applications.

Ni–YSZ is a common choice for the anode material of SOFCs in both electrolyte supported and anode supported geometries owing to its low-cost, thermal and chemical stability, good electronic conductivity, and high catalytic activity for hydrogen oxidation [1]. Providing intimate contact of ionic, electronic and pore phases at triple phase boundaries (TPBs) is critical to optimising electrochemical performance. In these composite porous anodes, TPBs are distributed throughout the electrode bulk.

Recently, the use of advanced focused ion beam (FIB) tomographic techniques has enabled direct access to information on the spatial distribution of TPBs in an SOFC electrode structure (e.g., [2–5]). The so-called TPB density, a measure of the abundance of TPB length per unit volume, is an important metric for the comparison of different electrode structures as it is generally viewed that a greater TPB density will increase electrode performance for a given materials set [6].

The electronic conductivity of Ni is typically several orders of magnitude higher than the ionic conductivity of YSZ [7]. As the electronic conductivity of YSZ is negligible under SOFC operating conditions, the transport of charged species will occur preferentially in the Ni phase and the electrochemically active region will be located in a region close to the electrode–electrolyte interface; Primdahl and Mogensen [8] estimate the active thickness for Ni–YSZ anodes to be under 20 μm. Therefore there is diminishing benefit in continuing to increase electrode thickness in order to maximise the number of triple phase boundaries [9], as much of the added thickness will be electrochemically inert. However, questions remain regarding the optimum thickness for a given electrode structure and material.

In composite electrodes, the distribution of triple phase contacts throughout the electrode bulk allows distributed current generation in a 3D volume. As the fuel cell community places increasing emphasis on the importance of microstructure for electrochemical optimisation, it is essential that relevant electrochemical param-

* Corresponding author at: Department of Earth Science and Engineering, Prince Consort Road, RSM Building, London SW7 2AZ, UK. Tel.: +44 020 75945704; fax: +44 020 75947444.
E-mail addresses: p.shearing@imperial.ac.uk (P.R. Shearing), q.cai@imperial.ac.uk (Q. Cai), j.golbert@imperial.ac.uk (J.I. Golbert), v.yufit@imperial.ac.uk (V. Yufit), c.adjiman@imperial.ac.uk (C.S. Adjiman), n.brandon@imperial.ac.uk (N.P. Brandon).

0378-7753/$ – see front matter © 2010 Elsevier B.V. All rights reserved.
doi:10.1016/j.jpowsour.2010.02.047

Nomenclature

f_n	material fraction
K_n	conductivity (S m^{-1})
ϕ_n	volume fraction
V_n	potential (V)
ρ_{TPB}	TPB density (μm^{-2})
R	gas constant (J mol^{-1} K^{-1})
T	temperature (°C)
F	Faraday's constant (C mol^{-1})
j	charge transfer current per unit length (A μm^{-1})
x	distance from interface (boundary condition)
pH_2	partial pressure
η	over-potential (V)
β	transfer coefficient = 0.5
D_{H_2}	diffusivity (m^2 s^{-1})
E_{io}	ionic activation energy (J mol^{-1})
E_A	activation energy for hydrogen oxidation (J mol^{-1})
γ	pre-exponential factor (A μm^{-1})
σ_{io}	ionic conductivity (S m^{-1})
R_{CT}	charge transfer resistance (A cm^{-2})
z	number of electrons transferred
EIS	electrochemical impedance spectroscopy
TPB	three phase boundary

eters can be quantified. A key measure of electrode performance is the exchange current density which provides a measure of the propensity of a given electrode material to catalyse an electrode reaction at a given temperature.

In order to effectively compare the electrochemical performance of composite electrodes, exchange current density should be considered per unit volume, or per unit length of TPB. Obtaining such data is difficult, but experiments using geometrically defined, dense Ni structures on YSZ substrates [6,10] have provided some electrochemical data, reported per unit length of TPB.

Modelling of fuel cells over many length scales from fundamental electrochemistry [11], through cell level [7,12,13], to system and stack level [14–16] provides valuable insight, allowing us to explore operation under steady state and transient conditions. Models also afford easy manipulation of variables and observation of their effects; this information can be used to predict and enhance cell performance. Numerical simulations provide valuable information on cell stress, potential, current density and temperature in electrodes and may also predict the effects of changes in microstructural parameters on electrode percolation and performance [7,17].

Models that explore phenomena at the cell level require information on the microstructural framework so that the electrochemical simulation can be performed; this may be in two [18] or three [7,17] dimensions. The generation of microstructures that are representative of real systems is currently the subject of a significant research effort.

Numerical generation is one possible route to obtaining these frameworks, for example using Monte Carlo techniques to approximate the packing of the three constituent phases [19]. The complexity and accuracy of the frameworks derived in this manner varies greatly; however, mono-disperse, homogenous and spherical particles are common assumptions (e.g., [18]). More complex models may also consider the effects of sintering on the material microstructure (e.g., [7,17]), but such techniques can be computationally expensive and are constrained by a limited understanding of the evolution of actual microstructures during sintering processes.

The availability of accurate information concerning the 3-dimensional distribution of TPBs in an electrode, for example from FIB tomography, provides an opportunity to combine experiment with simulation. By mimicking experimental microstructures computationally, one gains the ability to compare experimental results with the output of electrochemical simulations, thereby offering a potential tool for model validation. In turn, this will improve the accuracy of the simulation which may then be used to design optimum electrode microstructures.

In this paper we present work to combine experimental electrochemical and microstructural characterisation with electrochemical simulation. Using a standard, electrolyte supported, screen printed Ni–YSZ anode, electrochemical impedance spectroscopy has been conducted in a symmetrical cell configuration. The electrode microstructure has been characterised using FIB tomography and the resulting microstructure has been used as the basis for electrochemical simulation. The outputs from this simulation have in turn been compared to the results of the electrochemical experiments.

2. Part 1—experimental

Ni–YSZ symmetrical cells of 11 mm diameter have been prepared by screen printing commercially available NiO–YSZ ink (Cerampaste manufactured by Ceramtec) onto commercially available pre-sintered, tape cast YSZ pellets (Nextech Materials). The single layer screen printed anodes were then sintered at 1350 °C. Reduction of NiO to Ni followed the manufacturers' guidelines: cells were heated to 600 °C in 97% N_2, 3% steam, at 600 °C, the concentration of H_2 was increased to 97% over a period of 1 h, where the cells were held for 1 h before cooling in N_2.

Electrochemical impedance spectroscopy (EIS) has been used to characterise the electrochemical performance of the cells at open circuit. EIS was performed in a symmetrical cell configuration using an Autolab Impedance Analyser system (PGSTAT30-Eco Chemie). EIS scans from 100 mHz to 1 MHz were carried out at temperatures ranging from 800 to 1000 °C in gas environments with H_2 varying from 48 to 97% with 3% steam, at a total gas flow rate of 100 ml$_n$ min^{-1}. Equivalent circuit analysis was performed using ZView2 (Scribner).

FIB tomography was used to characterise the Ni–YSZ electrode microstructure after electrochemical characterisation had been performed. A Zeiss xB-1540 FIB-FEG SEM was used in this study. The ion and electron beams were separated by 52° allowing simultaneous milling and imaging to be performed.

Prior to imaging, the electrode surface was carefully prepared in order to minimise negative effects such as streaking and redeposition. By maximising the quality of the raw images obtained, it has been possible to conduct automated image analysis of the resulting data set. To do this the entire sample was sputter coated with gold and firmly attached to a microscopy stub using silver paint, thereby providing a low resistance path to earth to dissipate the electronic beam current and prevent charging. Once an area of interest was identified, a thin layer of Pt was deposited onto the local electrode surface using a standard FIB gas injection system; the Pt layer serves to minimise streaking or curtaining effects that arise due to the incidence of the ion beam on a non-uniform tomography [20].

Using high beam currents, a U-shaped trench was then milled around the deposited Pt, as outlined in Fig. 1. The trench prevents milled material becoming re-deposited on the face of interest. Finally, the face of interest is polished using low-beam currents to remove any re-deposited material.

Through optimisation of the sample preparation procedure for charge dissipation, and by using improved automated image anal-

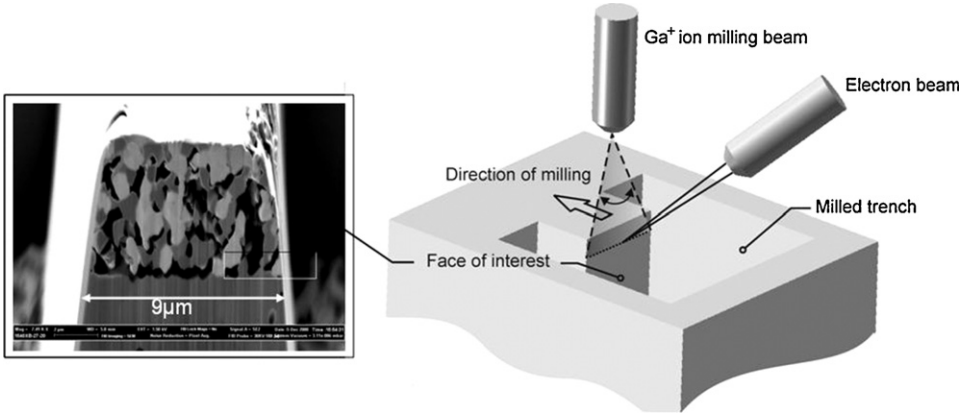

Fig. 1. Schematic illustration of the FIB milling technique, along with a typical image from the anode section.

ysis procedures, it was not necessary to perform the lift-out sample preparation technique described in our previous study [4].

Using the Zeiss xB1540, it is possible to collect tomography data in two ways, firstly by milling and imaging continuously, capturing images whilst the ion beam is still incident in the area of interest. However whilst this technique has the advantage of speed, it is sometimes possible to observe signal noise due to the interference of the ion and electron beams. The second method is to periodically interrupt milling whilst an image is captured; resuming once the electron beam scan has been completed. Both processes are fully automated. In this study the second method of image collection was adopted.

Milling was conducted at 100 pA with ion beam accelerating voltages of 30 kV. Low voltage imaging was conducted below 2 kV to maximise the contrast differential between Ni and YSZ [21]. The largest e-beam aperture was used to flood the electrode surface with electrons providing some charge equalisation for the incident, positively charged ion beam [22]. The low accelerating voltage also minimises the electron beam penetration volume [23] which minimises the out-of-plane information obtained from the porous substrate.

A sequence of 170 images was collected; pixel dimensions of 20 nm have been recorded with an inter-slice thickness of 15 nm. From this sequence, 100 images have been selected and segmented for further analysis. The images have been collected in SE2 (secondary electron) mode and demonstrate a good contrast gradient between the Ni and YSZ phase; using the SE2 mode, twin boundaries in the Ni have not been observed, which were problematic in other studies using back scatter detectors [4].

Image analysis has been performed using Matlab and Amira software. Images are manually aligned with reference to the sample edges (see Fig. 1) before they are cropped. An edge preserving smoothing filter is applied in 3D before the images are thresholded based on the image histogram, corresponding to the secondary electron yield. This segmentation process has a recurrent artefact; material along the outside edge of Ni grains has been erroneously identified as YSZ. This problem arises at the edge of material grains because of the high contrast gradient and is removed using mathematical morphology operations in Matlab [24]. Further information regarding the application of this technique and its accuracy are provided in Ref. [4].

Once the images have been successfully segmented, they are combined into a single 3D matrix which is then analysed for percolating three phase boundary contact. The calculation framework used has been presented by Golbert et al. [7], and the application to FIB serial section data is also presented in [4]. In this case the grid dimensions used are dependent on the voxel volume of the raw data.

3. Part 1—results and discussion

Electrochemical impedance spectroscopy was carried out in symmetrical cell configuration at temperatures from 800 to 1000 °C; results of the EIS are presented in Fig. 2.

Fig. 2(a) shows the EIS response for varying temperature in 97% H_2, 3% steam, on a molar basis. Fig. 2(b) shows the effect of varying H_2 concentration from 48 to 97% at 900 °C: impedance spectra were collected over the frequency range 100 mHz to 1 MHz.

As spectra in both figures suggest, three major processes can be identified at high, middle and low frequencies. The lowest error equivalent circuit fit has been obtained by implementing a model

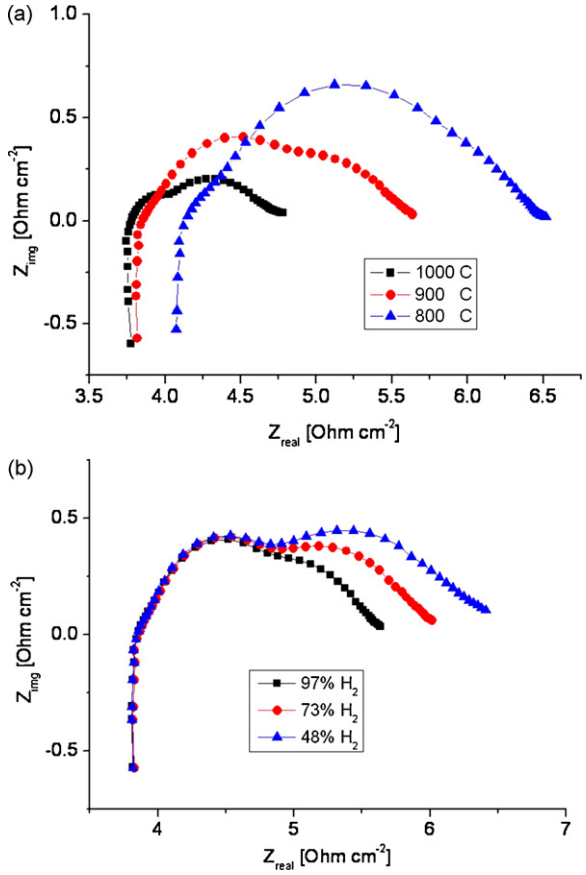

Fig. 2. (a) EIS scan for Ni–YSZ anode symmetrical cell at 800, 900 and 1000 °C (97% H_2, 3% steam diluted with N_2) and (b) EIS scan for Ni–YSZ anode symmetrical cell at 900 °C in varying H_2 concentration (48–97% H_2).

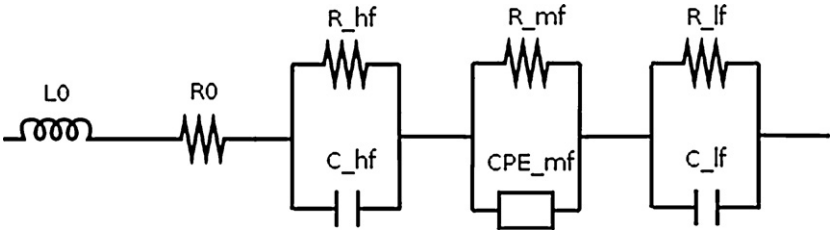

Fig. 3. Equivalent circuit analysis for electrode processes.

Table 1
Area specific resistances extracted from EIS data.

Temperature [°C]	H_2 (%)	R_{HF} [Ω cm^2]	R_{MF} [Ω cm^2]	R_{LF} [Ω cm^2]
1000	97	0.08	0.86	0.16
1000	73	0.09	1.45	0.21
1000	48	0.09	2.06	0.27
900	97	0.39	1.37	0.14
900	73	0.39	1.71	0.20
900	48	0.40	2.14	0.23
800	97	0.80	1.54	0.17
800	73	1.05	2.19	0.29
800	48	1.06	2.76	0.29

with two capacitors and one constant phase element, each in parallel with a resistor, as indicated by Fig. 3. Fitting data of area specific resistances for three processes are collected in Table 1, the mean error for the least square fitting was less than 0.03% per arc.

According to the data, the high frequency process is greatly affected by temperature and seems to be largely independent of hydrogen concentration. Such behaviour is consistent with a thermally activated charge transfer reaction, reported to be a two-electron process ([25,26]). Two other processes are identified at medium and low frequency and are shown to be affected by hydrogen concentration, and less sensitive to temperature, especially at the lowest frequency. These processes are associated with diffusion phenomena [27,28].

From the FIB tomography sequence, 100 slices have been segmented and analysed, using a voxel dimension of 20 nm × 20 nm × 15 nm corresponding to a sample size of 6.68 μm × 5.04 μm × 1.50 μm. Whilst larger reconstructions have been conducted (e.g., [3,4]) this volume is representative of the screen-printed electrode which has a thickness of 5 μm.

Fig. 4 shows the reconstructed anode, which has a total sample size of 6.68 μm × 5.04 μm × 1.50 μm.

Within the co-ordinate geometry of the electrode, a contiguous ionic pathway is required between the electrolyte and TPB, and the gas and electronic phases must be percolated between the TPB and current collector/gas bulk. The reconstructed volume has been arbitrarily labelled in the 3D Cartesian system with the volume 6.68 μm × 5.04 μm × 1.50 μm corresponding to the *x*, *y* and *z* dimensions, respectively. The reconstruction encompasses the full electrode thickness, labelled here as the *y*-plane. The percolation of the constituent phases must be considered in the *y*-dimension in agreement with the required co-ordinate geometry discussed above. However, because the direction of milling (see Fig. 1) is not defined relative to the co-ordinate geometry of the electrode in the *x*–*z* plane, percolation must be considered in both the *x*–*y* and *y*–*z* planes. This factor can be used to assess whether the sample is sufficiently large by considering the homogeneity of the reconstructed samples relative to the bulk electrode; whilst the total TPB density will be the same irrespective of the direction of percolation, a homogenous sample should demonstrate similar percolated TPB density in both the *x*–*y* and *y*–*z* planes. Where the reconstructed volume is too small relative to the sintered particle size distribution, percolation will be restricted in one plane because the enhanced percolation in a single phase will prevent percolation of the remaining phases. For example, a large Ni grain relative to the dimension of the reconstructed volume will promote electronic conductivity, but by virtue of its high volume fraction will hinder gas and ionic phase percolation, reducing the number of percolated TPBs.

In this sample, a total TPB density of 12.99 μm^{-2} was calculated, of which 8.15 μm^{-2} is percolated in the *x*–*y* plane (percolation of 63%) and 9.34 μm^{-2} is percolated in the *y*–*z* plane (percolation of 72%). This broad agreement in percolation in both planes lends weight to the homogeneity and therefore the statistical relevance of the reconstructed volume.

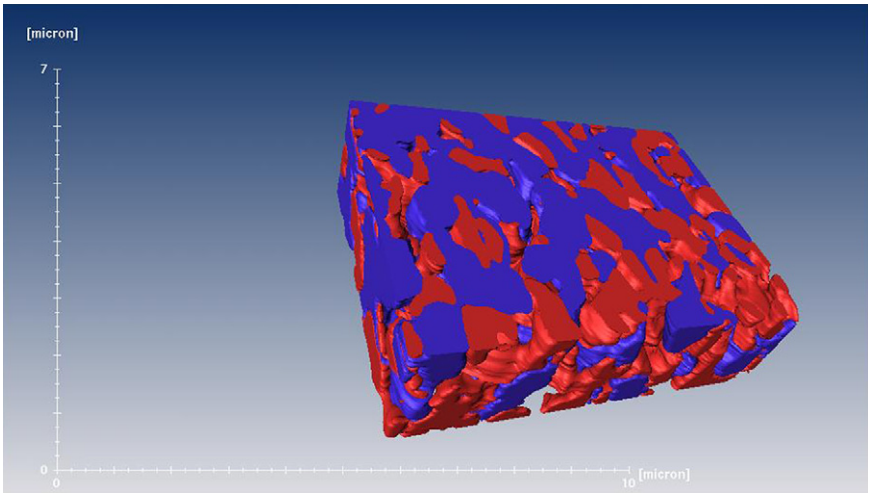

Fig. 4. 3D reconstruction of Ni–YSZ anode—red corresponds to YSZ phase, blue to Ni and pore space is void. Total sample volume is 6.680 μm × 5.040 μm × 1.50 μm. (For interpretation of the references to color in this figure legend, the reader is referred to the web version of the article.)

In Part 2 of this work, the application of the experimentally obtained structure as the basis for an electrochemical simulation is considered, and the estimation of the length-specific exchange current is presented (exchange current per unit TPB length). The length-specific exchange current has also been extrapolated from literature results for model anode geometries; its calculation and comparison are also presented in order to provide a validation of the experimentally derived structure.

4. Part 2—electrochemical simulation

Transport phenomena in porous electrodes are intimately linked to electrode microstructure; specifically to the porosity, the pore size and the tortuosity factor. In order to capture this behaviour, the transport phenomena are modelled for each phase separately and linked at the percolated TPB, where charge transfer occurs. For transport modelling, the microstructure is divided into voxels, with each voxel represented as a cube of pixels. Each voxel contains different volumes of the three phases. Using the VOF methodology [29], the phase fractions in a voxel i are represented by $f_{i,\mathrm{pore}}$, $f_{i,\mathrm{io}}$, and $f_{i,\mathrm{el}}$, for the pore, ionic and electronic phases, respectively. The characteristics of a voxel i, for example its conductivity κ_i, are assumed to be dependent on the characteristic values in the pure phases (e.g., κ_n^o, n = pore, io, el) and the phase fractions in that voxel:

$$\kappa_i = \sum_n \kappa_n^o f_{i,n} \tag{1}$$

Note that materials with mixed conductivity can be handled in this framework (for example, anodes using CGO rather than YSZ), since each material can have a different conductivity for each charged species. In this paper, we assume that each phase conducts only one species. Assuming steady state and ideal gases in the pores, and considering only the diffusion of H_2 and H_2O, we model the ionic and electronic potentials in an SOFC anode using the following system of equations:

$$\nabla(\sigma_{\mathrm{io}} f_{\mathrm{io}} \nabla V_{\mathrm{io}}) = -\rho_{\mathrm{TPB}} j \tag{2}$$

$$\nabla(\sigma_{\mathrm{el}} f_{\mathrm{el}} \nabla V_{\mathrm{el}}) = 2\rho_{\mathrm{TPB}} j \tag{3}$$

$$\nabla\left(\frac{D_{\mathrm{H_2O}} f_{\mathrm{pore}}}{RT} \nabla P_{\mathrm{H_2O}}\right) = \rho_{\mathrm{TPB}} \frac{j}{2F} \tag{4}$$

$$\nabla\left(\frac{D_{\mathrm{H_2}} f_{\mathrm{pore}}}{RT} \nabla P_{\mathrm{H_2}}\right) = -\rho_{\mathrm{TPB}} \frac{j}{2F} \tag{5}$$

where ρ_{TPB} is the local TPB density (in $\mu\mathrm{m}\,\mu\mathrm{m}^{-3}$) and j is the charge transfer current per unit TPB length, σ_{io} and σ_{el} are the ionic conductivity and the electronic conductivity, respectively, $D_{\mathrm{H_2O}}$ and $D_{\mathrm{H_2}}$ are the diffusion coefficient of H_2O and H_2, respectively, f_{io}, f_{el} and f_{pore} are the volume fraction of ion conducting, electron conducting and pore phases, V_{io} and V_{el} are the ionic potential and the electronic potential, respectively, $P_{\mathrm{H_2O}}$ and $P_{\mathrm{H_2}}$ are the partial pressure of H_2O and H_2, F is the Faraday constant, R is the gas constant, and T is the temperature. All quantities expect for F and R depend on the position (x, y, z).

These phenomena are modelled in each voxel i, and the volume-averaged values are taken over all the voxels. When integrating Eqs. (2)–(5), a small-enough step of 1×10^{-8} is taken in the variables for finite differencing so as to avoid errors. V_{io} can be integrated from 0 V up to 1.23 V, depending on the operating temperature. The electronic conductivity of Ni (σ_{el}) is assumed to be high enough to neglect its electronic resistance, so the electrode potential, V_{el}, is assumed to be zero throughout the electrode. Both $P_{\mathrm{H_2O}}$ and $P_{\mathrm{H_2}}$ can be integrated over the range 0–1.

The boundary conditions are as follows: it is assumed that the electrode/current collector interface (ion insulating) is at $x = 0$ and the electrode/electrolyte interface (electron insulating and impermeable to gas) is at $x = L$. $P_{\mathrm{H_2O}}, \infty$ and $P_{\mathrm{H_2}}, \infty$ indicate the partial pressure of H_2O and H_2 at the inlet. All the boundaries at the directions of y and z are assumed to be insulating.

In our model, charge transfer is assumed to be the rate determining electrode process, and thus the Butler–Volmer equation is used to calculate the current density as shown by Eq. (6), where $\beta = 0.5$ and j_0 is exchange current per TPB length in A $\mu\mathrm{m}^{-1}$.

$$j = j_0 \left(\exp\left(\frac{2\beta F}{RT}\eta\right) - \exp\left(-\frac{2(1-\beta)F}{RT}\eta\right)\right) \tag{6}$$

For the SOFC anode there is a relation for the potential terms as below:

$$V_{\mathrm{eq}} - \eta = V_{\mathrm{io}} - V_{\mathrm{el}} \tag{7}$$

where η is the over-potential, V_{io} the ionic potential, and V_{el} the electronic potential, and V_{eq} is the potential at equilibrium, defined by Eq. (8):

$$V_{\mathrm{eq}} = V_{\mathrm{oe}} - \frac{RT}{2F}\ln\left(\frac{P_{\mathrm{H_2O}}}{P_{\mathrm{H_2}}}\right) \tag{8}$$

V_{oe} is the standard potential which is determined as a function of the Gibbs free energy change involved in the reaction, taking the partial pressures of H_2, H_2O and O_2 to be at standard pressure. The variation of V_{oe} over the temperature range of 800–1000 °C is calculated using the following equation [30]:

$$V_{\mathrm{oe}} = 1.23 - 2.304 \times 10^{-4}(T - 298.15) \tag{9}$$

Combining Eqs. (7) and (8) gives an expression for the over-potential:

$$\eta = V_{\mathrm{eq}} - (V_{\mathrm{io}} - V_{\mathrm{el}}) = V_{\mathrm{oe}} + V_{\mathrm{el}} - V_{\mathrm{io}} - \frac{RT}{2F}\ln\left(\frac{P_{\mathrm{H_2O}}}{P_{\mathrm{H_2}}}\right)$$

$$= V_{\mathrm{oe}} + V_{\mathrm{el}} - V_{\mathrm{io}} + \frac{RT}{2F}\ln\left(\frac{P_{\mathrm{H_2}}}{P_{\mathrm{H_2O}}}\right) \tag{10}$$

Substituting (10) into (6) results in a definition of the charge transfer current as a function of the state variables:

$$j = j_0 \left[\exp\left[\frac{F}{RT}(V_{\mathrm{oe}} + V_{\mathrm{el}} - V_{\mathrm{io}})\right]\sqrt{\frac{P_{\mathrm{H_2}}}{P_{\mathrm{H_2O}}}} - \exp\left[\frac{-F}{RT}(V_{\mathrm{oe}} + V_{\mathrm{el}} - V_{\mathrm{io}})\right]\sqrt{\frac{P_{\mathrm{H_2O}}}{P_{\mathrm{H_2}}}}\right] \tag{11}$$

The ionic conductivity, σ_{io}, is estimated by using Eq. (12) [31]:

$$\sigma_{\mathrm{io}} = \frac{\sigma_{\mathrm{io}}^0}{T}\exp\left(-\frac{E_{\mathrm{io}}}{RT}\right) \tag{12}$$

where $\sigma_{\mathrm{io}}^0 = 3.6 \times 10^7\ \mathrm{S\,m^{-1}}$ is the pre-exponential factor (or reference ionic conductivity) and $E_{\mathrm{io}} = 8.0 \times 10^4\ \mathrm{J\,mol^{-1}}$ is the activation energy for the ionic transport [32].

The system of equations represented by Eqs. (2)–(5), (10), (11) and the boundary conditions in Table 2 is solved by developing mass/charge balances for each voxel surrounding the discretization points, using the finite volume method [29]. The details of the solver methodology can be found elsewhere [7]. The input parameters used are given in Table 3.

The exchange current per unit TPB length, j, is fitted using an iterative approach. The current density-over-potential response predicted by the electrochemical model for the given SOFC anode microstructure and a given value of the exchange current per unit

Table 2
Electrochemical simulation boundary conditions.

@ $x=0$	@ $x=L$
$\partial V_{io}/\partial x = 0$	$V_{io} = 0 - 1.23$
$V_{el} = 0$	$\partial V_{el}/\partial x = 0$
$P_{H_2O} = P_{H_2O}, \infty$	$\partial P_{H_2O}/\partial x = 0$
$P_{H_2} = P_{H_2}, \infty$	$\partial P_{H_2}/\partial x = 0$

Table 3
Electrochemical simulation input parameters. In this work, length-specific exchange current is used as a fitting parameter (see text).

Temperature (°C)	800	900	1000
Ionic conductivity (S μm^{-1})	4.28×10^{-6}	8.40×10^{-6}	14.7×10^{-6}
Electronic conductivity (S μm^{-1}) [33]	2.4	2.17	1.85
D_{H_2} (m^2 s^{-1}) [34]	4.11×10^{-5}	4.11×10^{-5}	4.11×10^{-5}
D_{H_2O} (m^2 s^{-1}) [34]	4.11×10^{-5}	4.11×10^{-5}	4.11×10^{-5}
V_{oe} (V)	1.05	1.028	1.005

length is used to obtain a predicted area specific resistance for charge transfer. This value is compared to the area specific resistance for charge transfer as estimated from EIS measurements (R_{HF} in Table 1). The exchange current per unit length is adjusted until good agreement is obtained.

The following procedure is used to compute the area specific resistance for charge transfer. At low over-potentials, it is possible to assume straight line behaviour for the current–voltage response according to the low-field Tafel approximation [8], which assumes charge transfer limited (Butler–Volmer) kinetics. The gradient of the voltage–current density plot at low over-potential ($\eta < 20$ mV) therefore defines the charge transfer resistance.

By performing the simulation procedure outlined here, the exchange current per unit TPB length for a Ni–YSZ system in 97% H_2, 3% steam has been calculated at three different temperatures. The length-specific exchange current is estimated to be 9.4×10^{-11}, 2.14×10^{-10} and 1.22×10^{-9} A μm^{-1} at 800, 900 and 1000 °C, respectively. Fig. 5 shows the results of this iterative procedure at three temperatures at which the area specific resistances are 0.803 Ω cm^2, 0.387 Ω cm^2 and 0.076 Ω cm^2, respectively, corresponding well to the experimentally measured charge transfer resistances shown in Table 1, i.e. R_{HF}. This part of the EIS response is appropriate for comparison as our electrochemical model currently considers only electron transfer; we do not yet account for

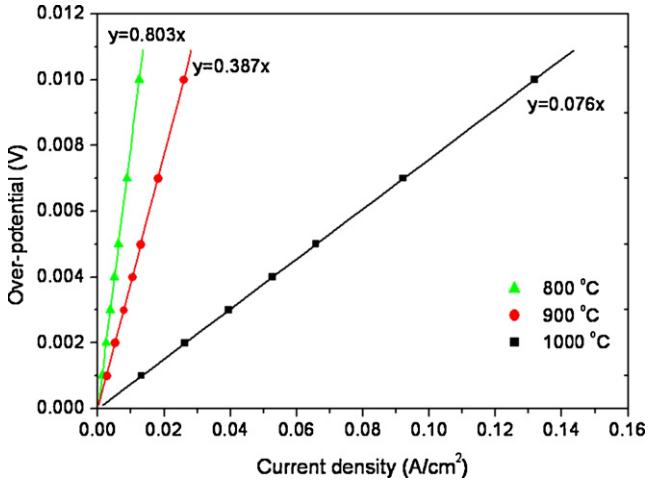

Fig. 5. Over-potential as a function of current density (normalised for geometrical electrode area) as predicted by electrochemical simulation (data points from electrochemical simulation, straight line approximation provides ASR).

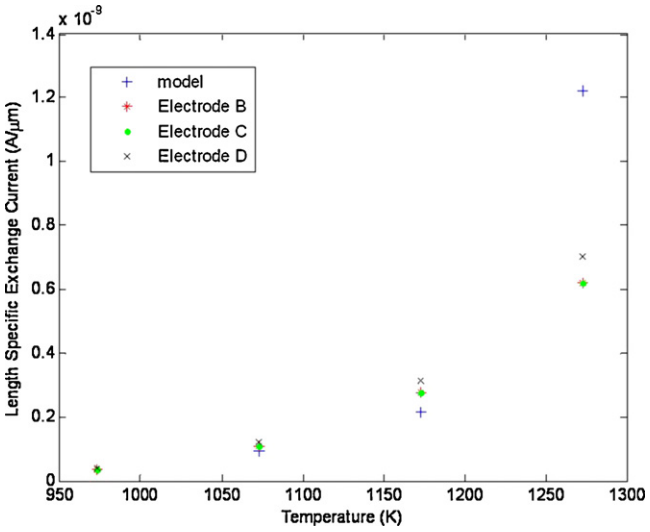

Fig. 6. Calculated variation of length-specific exchange current with temperature for different geometrically defined electrodes at open circuit.

additional contributing processes such as adsorption and surface diffusion, which will be considered in future studies.

In principle, the fitted values of the exchange current density can be compared to experimental data obtained using dense, geometrically defined Ni electrodes, deposited on a smooth YSZ surface. This enables the isolation of triple phase contact points, the length of which may be subsequently measured. In doing so, electrochemical measurements can be directly correlated with TPB length. However there are very few such data sets reported in the literature. Bieberle et al. [6] have deposited dense Ni by magnetron sputtering onto a YSZ single crystal surface. The deposited Ni was subsequently patterned using photo-lithography to alter the effective TPB length. Four model electrode samples were prepared, with TPB lengths ranging from 0.04 to 8.738 m (labelled here as electrodes A–D). Using data reported by Bieberle et al., it has been possible to extrapolate data on the length-specific exchange current; the calculation method is outlined here.

Fig. 11 from Bieberle et al. [6] shows the variation of polarisation resistance with TPB length. For the geometrically defined system, it is assumed there is no diffusion limitation and the resistance is therefore attributed to charge transfer only. Using the following equation it is possible to extract the exchange current density from the polarisation resistance assuming Butler–Volmer kinetics. This allows direct comparison with the length-specific exchange current density obtained from the model assuming Butler–Volmer kinetics:

$$j_0 = \frac{R \cdot T}{z \cdot R_{CT} \cdot F} \tag{13}$$

The temperature dependence of exchange current per unit length is extrapolated using:

$$j_0 = \dot{\gamma} \cdot \exp\left(\frac{-E_A}{RT}\right) \tag{14}$$

where E_A is the activation energy and z is the number of electrons transferred. The pre-exponential factor is calculated from the experimental data obtained at 800 °C. Literature values for the activation energy of hydrogen oxidation at nickel electrodes [32] were used to extrapolate the behaviour of exchange current with temperature, this is shown in Fig. 6. By extrapolating the changes in length-specific exchange current, it is possible to compare the experimental results with our predictions; this is shown in Fig. 6 and Table 4.

In Table 4, the exchange current per unit TPB length extrapolated from measured data (electrodes A–D) is presented alongside

Table 4
Temperature profile for length-specific exchange current: experimental data from Bieberle et al. (electrodes A–D) and predictions from our model.

Electrode	J_0 (A μm^{-1}) at temperature (°C)		
	800	900	1000
A	4.69E−10	1.22E−09	2.73E−09
B	1.07E−10	2.77E−10	6.21E−10
C	1.20E−10	3.13E−10	7.01E−10
D	1.21E−10	3.14E−10	7.02E−10
Model	0.94E−10	2.14E−10	12.2E−10

exchange current data predicted using the simulation presented here (labelled "model"). The predicted data can, in most cases, be seen to compare favourably with length-specific exchange current data extrapolated from the literature. The main difference that can be observed is for electrode A, which may reflect the small TPB length of this experimental sample (0.04 m) compared with the other patterned electrode samples (ranging between 2.5 and 8.7 m), which would be expected to increase experimental error. Consequently the value for electrode A was not used further in our analysis, but an average of electrodes B–D was used, namely 1.16×10^{-10}, 3.01×10^{-10}, and 6.75×10^{-10} A μm^{-1} at 800, 900 and 1000 °C, respectively.

Furthermore we note that Utz et al. [10] have recently suggested that for patterned Ni electrode geometries on YSZ substrates, increases in TPB length of up to 30% can be observed when heating the sample from room temperature to SOFC operating temperatures. This requires further study to refine these challenging measurements.

It is also evident from Table 4 that agreement between our extracted data and the experimental data is better at lower temperature. This is perhaps not surprising as we have assumed charge transfer to be rate determining, which will be more likely at lower temperatures, as evidenced by the higher charge transfer resistance reported for lower temperatures in Table 1.

5. Conclusions

The potential to link electrochemical and microstructural characterisation with electrochemical simulation has been explored. The estimation of length-specific exchange currents has been demonstrated using a combined modelling and experimental approach, which has compared favourably with the limited experimental data available from the literature.

A sample of an SOFC anode of 6.68 μm × 5.04 μm × 1.50 μm in size was imaged in three dimensions using focused ion beam techniques and the TPB density was found to be 12.99 μm^{-2}. This same anode was measured using electrochemical impedance spectroscopy, and the charge transfer resistance determined at temperatures of 800, 900 and 1000 °C.

An electrochemical anode model has also been used to represent the system using the imaged anode microstructure. The performance predicted by the model has been compared to the measured electrochemical performance, and the length-specific exchange current varied until agreement was reached between the predicted and measured performance, with the assumption that charge transfer was rate determining. The extracted length-specific exchange currents for hydrogen oxidation (97% H_2, 3% H_2O) at a Ni–YSZ anode were 0.94×10^{-10}, 2.14×10^{-10}, and 12.2×10^{-10} A μm^{-1} at 800, 900 and 1000 °C, respectively. These values are consistent with equivalent literature data for length-specific exchange currents for hydrogen oxidation at geometrically defined nickel electrodes on YSZ electrolytes; namely 1.16×10^{-10}, 3.01×10^{-10}, and 6.75×10^{-10} A μm^{-1} at 800, 900 and 1000 °C, respectively, noting that the increasing discrepancy between these two data sets with temperature may reflect the simplifying assumption made in this work that charge transfer is rate determining.

Future work is focused on fully validating the electrochemical simulations, with the aim of developing a powerful tool for electrode design. Furthermore, it should become possible to compare the results of 3D reconstructions of real electrodes with Monte Carlo simulations of electrode microstructures, allowing us to improve the accuracy of numerically generated electrode analogues. Work is also underway to expand the existing electrochemical simulations to extend the electrode kinetic model to include adsorption and surface diffusion processes.

Acknowledgements

This work is supported by the EPSRC Supergen Fuel Cells programme. Focused Ion Beam experiments were conducted at the London Centre for Nanotechnology. The authors also acknowledge EPSRC grant GR/T26344 for access to image processing and rendering software.

References

[1] J.W. Fergus (Ed.), Solid Oxide Fuel Cells: Materials Properties and Performance, CRC Press, 2009.
[2] D. Gostovic, et al., Electrochemical and Solid State Letters 10 (12) (2007) B214–B217.
[3] H. Iwai, et al., Journal of Power Sources 195 (4) (2010) 955–961.
[4] P.R. Shearing, et al., Chemical Engineering Science 64 (17) (2009) 3928–3933.
[5] J.R. Wilson, et al., Nature Materials 5 (7) (2006) 541–544.
[6] A. Bieberle, L.P. Meier, L.J. Gauckler, Journal of the Electrochemical Society 148 (6) (2001) A646–A656.
[7] J.I. Golbert, C.S. Adgiman, N.P. Brandon, Industrial Engineering Chemical Research 47 (20) (2008) 7693–7699.
[8] S. Primdahl, M. Mogensen, Journal of the Electrochemical Society 144 (10) (1997) 3409–3419.
[9] T. Kenjo, M. Nishiya, Solid State Ionics 57 (3–4) (1992) 295–302.
[10] A. Utz, et al., SOFC XI, ECS, Vienna, Austria, 2009.
[11] W.G. Bessler, Solid State Ionics 176 (11–12) (2005) 997–1011.
[12] D.F. Chen, et al., Journal of Power Sources 191 (2) (2009) 240–252.
[13] B. Kenney, et al., Journal of Power Sources 189 (2) (2009) 1051–1059.
[14] P. Aguiar, C.S. Adjiman, N.P. Brandon, Journal of Power Sources 147 (1–2) (2005) 136–147.
[15] J.I. Gazzarri, O. Kesler, Journal of Power Sources 176 (1) (2008) 138–154.
[16] A. Selimovic, J. Palsson, Journal of Power Sources 106 (1–2) (2002) 76–82.
[17] L.C.R. Schneider, et al., Electrochimica Acta 52 (1) (2006) 314–324.
[18] J. Deseure, et al., Journal of the European Ceramic Society 25 (12) (2005) 2673–2676.
[19] S. Sunde, Journal of Electroceramics 5 (2) (2000) 153–182.
[20] L.A. Gianuzzi, Introduction to Focused Ion Beams, 2005.
[21] K. Thyden, Y.L. Liu, J.B. Bilde-Sorensen, Solid State Ionics 178 (39–40) (2008) 1984–1989.
[22] P.S. Jorgensen, J.R. Bowen, 8th European Fuel Cell Forum, EFCF, Lucerne, 2008.
[23] P.J. Goodhew, F.J. Humprheys (Eds.), Electron Microscopy and Analysis, 2nd ed., Taylor Francis, 1988.
[24] R.C. Gonzales, R.E. Woods, S.L. Eddins, Digital Image Processing Using Matlab, vol. 1, 2nd ed., Upper Saddle River, Prentice Hall, 2004.
[25] M. Brown, S. Primdahl, M. Mogensen, Journal of the Electrochemical Society 147 (2) (2000) 475–485.
[26] S.P. Jiang, S.P.S. Badwal, Journal of the Electrochemical Society 144 (11) (1997) 3777–3784.
[27] S. Primdahl, M. Mogensen, Journal of the Electrochemical Society 146 (8) (1999) 2827–2833.
[28] V. Sonn, A. Leonide, E. Ivers-Tiffee, Journal of the Electrochemical Society 155 (7) (2008) B675–B679.
[29] H.K. Versteeg, W. Malalasekera, An Introduction to Computational Fluid Dynamics: The Finite Volume Method, 2nd ed., Pearson Educational Ltd., London, 2007.
[30] R. O'Hayre, al. et (Eds.), Fuel Cell Fundamentals, John Wiley & Sons, Chichester, UK, 2006.
[31] H. Zhu, R.J. Kee, Journal of Power Sources 117 (1–2) (2003) 61–74.
[32] Y. Zhao, C. Ou, J. Chen, International Journal of Hydrogen Energy 33 (15) (2008) 4161–4170.
[33] M. Yousuf, P.C. Sahu, K.G. Rajan, Physical Review B 34 (11) (1986) 8086–8100.
[34] R.H. Perry, D.W. Green (Eds.), Perry's Chemical Engineering Handbook, 7th ed., McGraw Hill, New York, 1997.